Main Manuscript for

Synchronicity transitions determine coupling fluctuations in a model of coupled oscillators with plasticity

Satoshi Kuroki [a,1] and Kenji Mizuseki [a]

[a] Department of Physiology, Osaka Metropolitan University Graduate School of Medicine, Asahimachi 1-4-3, Abeno-ku, Osaka, 545-8585, Japan

[1] To whom correspondence may be addressed.

Email: skuroki@omu.ac.jp

Author Contributions: S.K.: Conceptualization, Investigation, Visualization, Writing - original draft, Writing – review and editing, Funding acquisition; K.M.: Supervision, Writing – review and editing, Funding acquisition

Competing Interest Statement: The authors declare that they have no known competing financial interests or personal relationships that could have appeared to influence the work reported in this paper.

Classification: Systems Neuroscience

Keywords: Network reorganization, Plasticity, EI balance, Synchronization

This PDF file includes:

Main Text
Figures 1 to 5

Abstract

Sleep and rest are crucial to knowledge abstraction and creativity. During these periods, synapses undergo plastic modification, while neuronal activities are collectively synchronized, accompanied by large shifts in the excitation-inhibition (EI) balance. These phenomena differ from the learning processes that occur during task engagement. However, the detailed mechanism by which synchronized neuronal activity reshapes neural circuits through plasticity remains unclear. The Kuramoto model is used to study the collective synchronization of oscillators, including neurons. We previously proposed the EI-Kuramoto model, in which an EI balance was implemented in the Kuramoto model. The model alters its synchronicity based on the EI balance of the interaction strength. In this study, we further developed the EI-Kuramoto model by implementing Hebbian and homeostatic plasticity, leading to a plastic EI-Kuramoto model. Models with robust inhibition consistently showed desynchronization and stable coupling. Contrastingly, weaker inhibition produced a bistable synchronization state, in which couplings with intermediate strengths fluctuated, while strong couplings remained stable. Our findings suggest that the dynamic interplay between network activity and plasticity explains why stronger synapses in the brain exhibit greater stability than their weaker counterparts. Moreover, this mechanism facilitated network reorganization during sleep and rest.

Significance Statement

The reorganization of neuronal circuits during sleep and rest is essential for knowledge abstraction and creativity. These states involve synaptic plasticity and collective neuronal synchronization, accompanied by significant shifts in the excitation-inhibition (EI) balance. However, the precise mechanism through which synchronized activity reshapes neural circuits via plasticity remains unclear. We developed a novel computational model, the plastic EI-Kuramoto model, which incorporates both coupling plasticity and EI balance. Our model demonstrates that robust inhibition leads to desynchronization and stable coupling. In contrast, weaker inhibition induces bistable synchronization, in which the intermediate-strength couplings fluctuate, whereas strong couplings remain stable. These findings provide a fundamental mechanism for network reorganization during sleep and rest.

Main Text

Introduction

Empirical evidence suggests that brain activity during sleep and rest promotes memory consolidation, abstraction of knowledge, and the creation of new ideas (1, 2) through the reorganization of neural circuits (3, 4). This reorganization should differ from the learning process during task performance. Indeed, synaptic plasticity during sleep and rest improves task performance (5, 6).

Neuronal synchronization occurs in two distinct states. Collective neuronal firing is desynchronized during active wakefulness, including task engagement, movement, and attentional states, as well as during rapid eye movement (REM) sleep. These conditions are referred to as brain-activated states (7, 8) throughout this paper. In contrast, neuronal firing synchronizes during non-REM (NREM) sleep and quiet wakefulness, collectively termed brain-deactivated states (7, 8). The transition between these states is associated with shifts in the excitation-inhibition (EI) balance. Firing rates of inhibitory neurons and synaptic conductance of inhibitory synapses are significantly elevated during brain-activated states, while those of excitatory synapses show comparatively smaller changes (9–12). These observations suggest that, during brain-deactivated states, EI-balance-dependent changes in collective neuronal synchronization, together with synaptic plasticity, can influence network

reorganization. However, the detailed mechanisms by which neuronal synchronization in the brain-deactivated state reshapes the neural network structure remain unclear.

The collective synchronization of oscillators, including neurons, has been studied using a model of coupled oscillators. Among these, the Kuramoto model is considered to be the simplest framework (13, 14), and numerous variants have been proposed. One variant, the EI-Kuramoto model, incorporates the EI balance by dividing oscillators into excitatory and inhibitory groups and assigning four interaction types between them (15, 16). We have previously shown that tuning these four strengths toggles the network between synchronized, desynchronized, and bistable states, potentially reflecting a neuronal synchronization mechanism (16). That study, however, kept all coupling weight—defined in this paper as pair-specific interaction strengths—fixed and identical, and therefore did not address how the EI balance and its associated dynamical states influence plastic changes in the coupling weights.

In this study, we focused on Hebbian and homeostatic plasticity. Hebbian plasticity, based on the principle “fire together, wire together,” strengthens synapses between neurons that fire in close temporal proximity (17). In contrast, homeostatic plasticity regulates neuronal excitability and synaptic strength to maintain network stability, thereby preventing excessive excitation or quiescence (18). The interplay between these plasticity mechanisms enables the emergence of diverse neuronal functions and firing patterns (19–22). Previous studies have incorporated plasticity into Kuramoto models, enabling coupling weights to adapt based on the oscillator activity to examine their impact on system synchronization (23–33). However, these studies focused on promoting synchronization under a single dynamic state. The effects of different collective dynamics, induced by shifts in the EI balance, on plastic changes in the network remain unexplored.

To address these gaps, we developed the EI-Kuramoto model by implementing Hebbian and homeostatic plasticity into the coupling weights between excitatory oscillator unit pairs (referred to as plastic EI [pEI]-Kuramoto model). We observed that the network maintained robustness and minimal fluctuations in coupling strength when inhibition was strong, corresponding to the desynchronized state. Conversely, with weaker inhibition, corresponding to the bistable state, couplings with moderate weights tended to fluctuate, whereas couplings with strong weights remained stable. These findings on the network dynamics of the pEI-Kuramoto model may provide important insights into the mechanisms of neural networks in a brain-deactivated state.

Results

Establishment of the pEI-Kuramoto model. The pEI-Kuramoto model comprised two oscillator groups: excitatory units, referred to as excUnits, and inhibitory units, referred to as inhUnits. These specific terms clarify that the units represented excitatory and inhibitory factors in this model, not actual neurons or synapses. Four interaction strengths were assigned between the groups, with only excitatory-excitatory couplings (J_{ee}) being distributed and plastic. The other interaction strengths, K_{ii} (repulsive strength between inhUnits), K_{ei} (attractive strength from excUnits to inhUnits), and K_{ie} (repulsive strength from inhUnits to excUnits), were constant across time and cell pairs (Fig. 1A; see Materials and Methods). The interactions are modeled as zero-phase lag sine functions. The interactions from excUnits are purely attractive, while those from inhUnits are purely repulsive. Accordingly, the terms "excitatory" and "inhibitory" are used synonymously with "attractive" and "repulsive," respectively.

First, we investigated how the distribution of pair-specific excitatory-excitatory coupling weights J_{ee} affected the dynamics of the pEI-Kuramoto model in the absence of plasticity (Fig. 1B and C). In our previous study, we demonstrated that the Kuramoto model with EI balance (EI-Kuramoto model) exhibits three distinct dynamic states: synchronized, bistable, and desynchronized, depending on the balance between the constant values of the interaction strengths (16). In this study, J_{ee} followed a Gaussian distribution with a mean of μ_{Jee} and a standard deviation of σ_{Jee}, where σ_{Jee} was set to 0, 1/10, and 1/2 of μ_{Jee} (Fig. 1B). The collective synchronization was quantified using the order parameter R, which represents the magnitude

of the average vector between the oscillator units. In this simulation, regardless of the standard deviation value, all systems with a distributed J_{ee} also exhibited synchronized (high R), bistable (alternating high and low R), and desynchronized (low R) dynamics, as observed with constant (σ_{Jee} = 0) values (Fig. 1C).

Next, we incorporated plasticity into J_{ee} by applying Hebbian potentiation and homeostatic regularization plasticity rules (see Materials and Methods). Among the various methods available for implementing Hebbian plasticity in the Kuramoto model, we initially selected the simplest method: the cosine function (SI Appendix, Fig. S1A; see Materials and Methods) (23–25, 28, 32, 33). In this process, when a pair of excUnits exhibits closer phases, their J_{ee} coupling weight is potentiated. Simultaneously, the J_{ee} distribution was rescaled to maintain the initial mean and standard deviation, thereby preventing over potentiation through homeostatic regularization plasticity (see Materials and Methods). The system dynamics were evaluated using the parameter set (μ_{Jee} = 1, σ_{Jee} = 0.1, K_{ei} = 3, K_{ie} = 3, K_{ii} = 3), at which the system exhibited a desynchronized state in the absence of J_{ee} plasticity. Under the cosine rule, unit pairs with smaller phase differences acquire a larger J_{ee} weight. This rule causes the J_{ee} distribution, which was initially Gaussian, to become bimodal (SI Appendix, Fig. S1B). Plasticity also influences the distribution of oscillator units, making the distributions of both phase and phase difference become bimodal (SI Appendix, Fig. S1C), consistent with previous studies that incorporated the Hebbian rule into the Kuramoto model (23, 28). This bimodal distribution of the coupling weight deviates from the long-tailed skewed distributions typically observed in biological synaptic weights (12, 34, 35).

To address this discrepancy, we introduced an exponential-based Hebbian plasticity rule to adjust the decay rate (Sparseness γ) of the gain for the phase difference (Fig. 1D). We applied this rule to a range of parameter sets and evaluated the resulting J_{ee} distribution using skewness, kurtosis, and dip values, which quantify the distribution bimodality (36). Although J_{ee} distributions initially followed a Gaussian pattern, they transitioned into various bimodal or skewed forms (Fig. 1E and F). We also quantified the synchronization of the excUnits using the mean and standard deviation of the order parameter R_{exc} over time, denoted as $E[R_{exc}]_t$ and $S[R_{exc}]_t$, respectively. Plasticity in J_{ee} affects synchronization (Fig. 1G), resulting in uniform, bimodal, or unimodal phase and phase-difference distributions depending on the plasticity parameters (Fig. S1D). Moreover, the boundary of the statistical features of the J_{ee} distribution (Fig. 1E) appears to coincide with the synchronization boundary (Fig. 1G). For further analysis, we chose a parameter set that resulted in a long-tailed skewed J_{ee} distribution (Fig. 1F, top, magenta circle), which more closely reflects the synaptic weight distributions observed in the brain (12, 34, 35).

Coupling fluctuation increases in bistable synchronization state. We next investigated how the dynamic state affects coupling weight, focusing on the role of inhibition, which varies significantly across brain states (9–12), resulting in changes in EI balance (7, 37). To this end, we altered the EI balance of the pEI-Kuramoto model by manipulating the interaction strength from inhUnits. We unified K_{ie} and K_{ii} into a single parameter, K_i, to simplify the simulation, following the approach used in our previous study (16). We then examined how the J_{ee} fluctuations were associated with the K_i values, quantified as the standard deviation of J_{ee} over time ($S[J_{ee}]_t$; see Materials and Methods) (Fig. 2A and B). We determined the system's dynamic state by analyzing the time course of R_{exc}, (Fig. 2C and D), as previously described (16).

When K_i < 0.4, both the average ($E\{S[J_{ee}]_t\}_n$) and standard deviation ($S\{S[J_{ee}]_t\}_n$) of $S[J_{ee}]_t$ across unit pairs were almost zero (Fig. 2A and B), indicating no plastic changes in J_{ee}. In this K_i range, the system was in a synchronized state, characterized by high $E[R_{exc}]_t$ and low $S[R_{exc}]_t$ (Fig. 2C and D). The coupling weights between individual pairs exhibited no fluctuation over time after reaching the synchronized state (Fig. 2E and F, K_i: 0.1; SI Appendix, Movie S1).

As K_i increased, $E\{S[J_{ee}]_t\}_n$ also increased, peaking at K_i = 0.7, then decreased, and eventually stabilized around K_i = 1.5 (Fig. 2A). Meanwhile, the $S\{S[J_{ee}]_t\}_n$ continued to increase (Fig. 2B). For K_i values above 1.5, the system transitioned into a desynchronized state characterized by low $E[R_{exc}]_t$ and $S[R_{exc}]_t$ values (Fig. 2C and D). Strong or weak couplings remained stable over

time, whereas those of intermediate strength fluctuated (Fig. 2E, K_i: 1.5; SI Appendix, Movie S2). The system generated transient clusters of units coupled with strong J_{ee} weights (Fig. 2F, K_i: 1.5, the lower leftmost panel, t = 24). Over time, most units left these clusters, leaving only small, stable subsets of the clusters (Fig. 2F, K_i: 1.5, the lower panels, t = 29–50).

In the intermediate range ($0.4 < K_i < 1.5$), the system exhibited a bistable state with high $S[R_{exc}]_t$ (Fig. 2D). Notably, the $S[J_{ee}]_t$ was significantly higher in this bistable state (Fig. 2A). Similar to the desynchronized state ($K_i > 1.5$), the couplings with high or low weights were stable. However, the intermediate-weighted couplings fluctuated more (Fig. 2E and F, K_i: 0.8 and 1.0). Notably, the number of these intermediate fluctuating couplings was higher in the intermediate K_i range (Fig. 2E and F, K_i: 0.8 and 1.0; SI Appendix, Movies S3 and S4) than in the low and high K_i ranges. Thus, transitions in the dynamic state were accompanied by changes in the coupling-weight fluctuations. In particular, the bistable state tended to exhibit larger J_{ee} fluctuations.

Note that Hebbian plasticity affected the dynamic state of the pEI-Kuramoto model (SI Appendix, Fig. S2A), slightly shifting the bifurcation points between the synchronized and bistable states and the bistable and desynchronized states toward larger K_i values. Owing to this effect, we observed a small discrepancy from the state predicted by the eigenvalue-based classification for the EI-Kuramoto model (16) (data not shown). However, the overall trend of the state transition from synchronized to bistable and then to desynchronized as K_i values increased remained consistent across different Hebbian learning rates. The enhancement of synchronization induced by Hebbian plasticity was consistent with the findings of previous reports on Kuramoto models incorporating cosine-shaped Hebbian plasticity (28, 33). In contrast, σ_{Jee} did not affect the dynamic states (SI Appendix, Fig. S2B), consistent with the results in the absence of J_{ee} plasticity shown in Fig. 1C.

Strong-weighted couplings are stable while intermediate couplings fluctuate. We further investigated coupling weight fluctuations under conditions of slightly weakened inhibition from the desynchronized state, assuming intermediate brain states between brain-activated and deactivated states. We analyzed the individual J_{ee} coupling weights at selected points of K_i (K_i = 0.8, 1.0, and 1.5, red crosses in Fig. 2A–D, except K_i = 0.1). Histograms of $E[J_{ee}]_t$ (mean of J_{ee} over time for each pair of units) and $S[J_{ee}]_t$ also tended to shift toward higher values as K_i decreased (Fig. 3A and B). A scatter plot of $E[J_{ee}]_t$ and $S[J_{ee}]_t$ formed a characteristic "bow-shaped" distribution (Fig. 3C). In this two-dimensional distribution, data points near the minimum and maximum $E[J_{ee}]_t$ values had lower $S[J_{ee}]_t$ values, whereas intermediate $E[J_{ee}]_t$ showed a higher $S[J_{ee}]_t$. This pattern was consistent across all distributions for different K_i values. A similar phenomenon, the stabilization of strong couplings (e.g., synapses with large mushroom-shaped spines), has been observed in brain synapses (38–40).

Furthermore, the $S[J_{ee}]_t$ values tended to increase at intermediate $E[J_{ee}]_t$ values with decreasing K_i (Fig. 3C), suggesting that K_i can regulate the fluctuations in individual J_{ee} plastic couplings. At high K_i values in desynchronized states (K_i = 1.5, green dots), the couplings stabilize, whereas at low K_i values in bistable states (K_i = 1.0 and 0.8, orange and blue dots), the couplings of intermediate weights become unstable. The high J_{ee} coupling remained stable with small fluctuations, even when K_i was low. These dynamics appear to be a mechanism that preserves the coupling of particularly strong pairs and resets pairs of moderate weight, facilitating the reorganization of the network structure (Fig. 2E and 2F).

To enable a direct comparison with Figure 7A and 7B of (40), which report the relationship between spine volume and its changes in hippocampal slices, we quantified the change in coupling weight, ΔJ_{ee} (= $J_{ee}(t+\Delta t) - J_{ee}(t)$), as a function of its current value, J_{ee}, at each time step in our pEI-Kuramoto model (Fig. 3D and E). We pooled J_{ee} values and their changes ΔJ_{ee} across all excUnit pairs and time points, binned the J_{ee} values, and computed the mean and the standard deviation of ΔJ_{ee} for each J_{ee} bin ($E[\Delta J_{ee}]_{t,n}$ and $S[\Delta J_{ee}]_{t,n}$). In the desynchronized state (K_i = 1.5, green lines), $E[\Delta J_{ee}]_{t,n}$ was slightly but significantly positive for small J_{ee} (Wilcoxon signed-rank test, bin=[0.011,0.012), mean=1.1×10^{-8}, n=6,686,034, W=1.06×10^{13}, $p<1.0\times10^{-308}$), then decreased with increasing J_{ee}, reaching a local minimum near $J_{ee}\approx0.02$.

Subsequently, $E[\Delta J_{ee}]_{t,n}$ increased and approached zero around J_{ee}≈0.025 (Fig. 3D), a region corresponding to the peak of $E[J_{ee}]_t$ (Fig. 3A and C). $S[\Delta J_{ee}]_{t,n}$ increased monotonically over the same range of J_{ee} (Fig. 3E). These trends closely mirror observations in hippocampal slices and *in vivo* cortical imaging (40, 41). In comparison, the bistable regimes (K_i=0.8 and 1.0, orange and blue lines) showed large deviations in the mean change, $E[\Delta J_{ee}]_{t,n}$, either in the same direction (K_i=1.0, orange line) or the opposite direction (K_i=0.8, blue line) as the desynchronized state (Fig. 3D). Furthermore, the standard deviation, $S[\Delta J_{ee}]_{t,n}$, was generally elevated relative to the desynchronized state across the range of J_{ee} from 0.01 to 0.025 (Fig. 3E).

Factors determining coupling weight properties. To identify the parameters that determine the individual J_{ee} coupling properties ($E[J_{ee}]_t$ and $S[J_{ee}]_t$) shown in Fig. 3, we explored the candidate parameters (natural frequency difference $\Delta\omega$, initial phase difference $\Delta\theta$, and initial J_{ee} values of each excUnit pair) involved in J_{ee} fluctuations (Fig. 4). We colored the dots of $E[J_{ee}]_t$ vs. $S[J_{ee}]_t$ distribution (Fig. 3C) according to each parameter value (Fig. 4A–C). For statistical comparison, couplings were roughly categorized based on whether $E[J_{ee}]_t$ exceeded 0.018 (high $E[J_{ee}]_t$ group) or not (low $E[J_{ee}]_t$ group) because the correlation between $E[J_{ee}]_t$ and $S[J_{ee}]_t$ reversed around this point (Fig. 4D–F).

Regarding differences in the natural frequency $\Delta\omega$, most pairs in the high (>=0.018) $E[J_{ee}]_t$ group had relatively small $\Delta\omega$, whereas pairs with larger $\Delta\omega$ tended to be in the low (<0.018) $E[J_{ee}]_t$ group (Fig. 4A and 4D). In the low $E[J_{ee}]_t$ group, $S[J_{ee}]_t$ appeared to increase with increasing $\Delta\omega$ (Fig. 4A). The initial phase differences $\Delta\theta$ between the pairs were also significantly different between high and low $E[J_{ee}]_t$ groups (Fig. 4B and E). In the high $E[J_{ee}]_t$ group, most pairs exhibited small initial $\Delta\theta$, whereas in the low $E[J_{ee}]_t$ group, the initial $\Delta\theta$ were uniformly distributed. Additionally, we examined the effect of the initial J_{ee} coupling weight, which showed no noticeable bias (Fig. 4C) and followed a normal distribution for both high and low $E[J_{ee}]_t$ groups (Fig. 4F). Considering these results, pairs with small differences in natural frequency and initial phase positions maintained more stable and larger J_{ee} weights (Fig. 4G and H). Conversely, the initial J_{ee} weight was not an important factor in determining the stability and strength of the couplings.

Theoretical analysis of quasi-steady coupling weight distribution. We investigated the theoretical mechanism underlying the fluctuation of coupling weights J_{ee} by analyzing their distribution in a quasi-steady state, assuming $J_{ee,kj}(t+\Delta t) \approx J_{ee,kj}(t)$ (SI Appendix, Supporting Text). Although a true static steady weight distribution does not exist in the desynchronized or bistable states due to the non-constant phases of each oscillator unit, the desynchronized condition allows for a quasi-steady state, where the phase and weight distributions evolve on a sufficiently slow timescale, resulting in minimal fluctuation of the J_{ee} distribution. Under this assumption, the coupling weights do not change as a result of the plastic modulation in Eqs. M11 and M14, leading to the following relationship (SI Appendix, Eq. S3).

$$J_{ee,kj} = \hat{J}_{ee,kj} + c\exp\left(-\gamma\left|\Delta\theta_{kj}\right|\right) \quad (1).$$

$$c = \frac{\alpha(1-\beta)}{\beta}$$

The first term, $\hat{J}_{ee,kj}$, represents the value of $J_{ee,kj}$, which is rescaled with the homeostatic regulation plasticity rule so that the mean and variance become $\hat{\mu}_{Jee}$ an $\hat{\sigma}_{Jee}$, respectively. The second term is the Hebbian potentiation component, scaled by the ratio between the Hebbian and homeostatic plasticity learning rates c. This equation indicates that the weight $J_{ee,kj}$ depends on the distribution of $\hat{J}_{ee,kj}$ and the distribution of phase difference between unit k and j $\Delta\theta_{kj}$ ($c\exp\left(-\gamma\left|\Delta\theta_{kj}\right|\right)$). Assuming this rule remains applicable during the approach to a quasi-steady state, successive iteration of the update rule progressively integrates the second $\Delta\theta$-dependent Hebbian term into the J_{ee} distribution. Furthermore, the distribution of $\Delta\theta$ is dependent on that of θ (SI Appendix, Supporting Text). Therefore, when the weight dynamics are sufficiently slow, the J_{ee} distribution is determined by the phase distribution. Indeed, the characteristics of the J_{ee} distribution appear to be correlated with the synchronization state of the system, which reflects the shape of the phase distribution (Fig. 1E, 1F, and SI Appendix, Fig. S1). Specifically, a uniform phase (and phase difference) distribution (desynchronized

state) corresponds to a right-skewed, long-tailed J_{ee} distribution (magenta circle in Fig. 1E, F and S1D). A bimodal phase distribution corresponds to a bimodal J_{ee} distribution (green circle in Fig. 1E, F and S1D and the cos rule in Fig. S1B and S1C). A unimodal phase distribution (synchronized state) corresponds to a left-skewed J_{ee} distribution (yellow circle in Fig. 1E, F and S1D).

Next, we considered the change in the phase difference for a pair of excUnits, $\Delta\theta_{kj}$. Assuming that $J_{ee,kj}$ and $\Delta\theta_{kj}$ are constant, the following relationship can be derived from Eqs. 1 and M9 (SI Appendix, Eq. S18):

$$-\Delta\omega + F_{inh} - F_{exc}^{(-kj)} = -2\left\{\hat{J}_{ee,kj} + c\exp\left(-\gamma\left|\Delta\theta_{kj}\right|\right)\right\}\sin\left(\Delta\theta_{kj}\right) \quad (2).$$

$\Delta\omega$ is the natural frequency difference between units k and j, F_{inh} is the interaction strength from the inhUnits, and $F_{exc}^{(-kj)}$ is the interaction strength from the excUnits, except for units k and j. $F_{inh} - F_{exc}^{(-kj)}$ is the R_{exc}- and R_{inh}-dependent term; its direction can be either attractive or repulsive, depending on the phase configuration of the system (SI Appendix, Supporting Text). The right-hand side of this equation represents the interaction strength between units k and j, whereas the left-hand side represents the net forces of the other factors. A stable fixed point for $\Delta\theta_{kj}$ exists, where the functions for the left- and right-hand sides intersect (SI Appendix, Fig. S3).

On the right-hand side, the attractive force is driven by both the homeostatic set-point, $\hat{J}_{ee,kj}$, and the Hebbian potentiation term. Near $\Delta\theta\approx0$, the Hebbian effect is strong, yielding a large attractive force. As the phase difference $|\Delta\theta|$ increases, this Hebbian potentiation weakens, and the coupling weight relative position within the J_{ee} distribution falls to a lower value, causing an overall attractive force reduction.

On the left-hand side, while the influence of F_{inh} and $F_{exc}^{(-kj)}$ is limited in a desynchronized state where R_{exc} and R_{inh} are near zero, their impact becomes non-negligible in the bistable state, where these order parameters undergo periodic modulation. Sufficiently large fluctuations in these forces cause the stable fixed point to disappear or be substantially displaced, thereby leading to large fluctuations in the phase difference between the unit pair.

Cyclic modulation of inhibition. Finally, we varied K_i to mimic the sleep-wake cycle (7, 8). J_{ee} fluctuated (Fig. 5A, SI Appendix, Movie S5) in response to K_i modulation (Fig. 5B, top panel). R_{exc} alternated between the desynchronized and bistable states (Fig. 5B, middle), with corresponding changes in $E\{S[J_{ee}]_t\}_n$ (Fig. 5B, bottom). When K_i was high, the system was in a desynchronized state, and $E\{S[J_{ee}]_t\}_n$ was small. Conversely, when K_i was low, the system exhibited a bistable state, and $E\{S[J_{ee}]_t\}_n$ increased. These dynamics can be considered as modeling how the circuit structure is stabilized during the brain-activated state and destabilized during the brain-deactivated state, thereby promoting circuit reorganization.

Discussion

In this study, we extended the previously developed EI-Kuramoto model by incorporating Hebbian and homeostatic plasticity to establish the pEI-Kuramoto model and analyzed its dynamics. We propose that this model represents a continuous transition between the stabilization and reorganization of network structures, modulated by the desynchronized-bistable state cycle through inhibition (Figs 2–5). This study introduces a possible mechanism for preserving strong couplings and reorganizing network structures during brain-deactivated states, as viewed through the dynamics of collective oscillators.

Potential mechanism for network reorganization. Although the brain-deactivated state is often associated with synchrony, it is not uniformly synchronized. Near the transition between synchronized and desynchronized states, the dynamics tend to become irregular or weakly stable, as captured by two-population coupled-oscillator models (42, 43). Sleep onset can be formalized as a noisy saddle-node bifurcation (44), and macroscopic brain-state transitions are often argued to occur near the bifurcation point (45, 46). Beyond transition periods, even within sleep, the microarchitecture shows intrinsic instability, such as NREM-REM sleep cycle (3, 4, 7, 8), the cyclic alternating pattern in NREM sleep (47), UP–DOWN state alternations

(48, 49), and microarousals (50), which may reflect switching among synchronized and desynchronized states. These fluctuation-driven transitions during state changes and in brain-deactivated conditions align with the bistable regime of our model under reduced inhibition.

Preserving robust couplings while randomizing weaker ones simplifies the network, rendering it sparse. The choice of plasticity parameters, which yield a long-tailed coupling weight distribution (Fig. 1E and F), similar to that observed in the brain (12, 34, 35) and mirror EI balance during state transitions and in brain-deactivated states (9–12), appears to facilitate network sparsification. The selective preservation of strong synaptic connections is also frequently observed in the brain (38–40) and is understood through molecular mechanisms, including the dynamics of NMDA receptors (5, 51) and actin filaments (52). Our findings introduce a potential mechanism for sustaining strong coupling when viewed from another aspect of the dynamic system of collective oscillators. Additionally, our results may be mechanistically linked to the systems-level observation that only a few neuronal populations remain stable, while others drift (53–55). This process aligns with the pruning method used in artificial neural networks, which facilitates knowledge generalization (56, 57). This pruning-like mechanism is particularly relevant when synaptic downregulation is dominant during brain-deactivated states (5, 51), as fluctuations in couplings can weaken the weights and eventually reset them to baseline.

Fluctuations in network connectivity can promote network reorganization. In our model, bistable states under low inhibition conditions, mirroring the EI balance during state transitions and brain-deactivated states (9–12), promoted fluctuating coupling weights between excUnits. It has also been proposed that the brain enhances neuronal circuit reorganization during the brain-deactivated state (3, 4). Combined with unknown mechanisms to evaluate and stabilize reorganized circuits (58), such as dopaminergic signaling during NREM sleep (59), which can provide a reinforcement-like signal and gate plastic changes, we may gain insights into how new creative ideas or innovative problem-solving methods are generated during the brain-deactivated state.

Dynamics of the pEI-Kuramoto model. The characteristic "bow-shaped" relationship between the mean ($E[J_{ee}]_t$) and standard deviation ($S[J_{ee}]_t$) of the coupling weights (Fig. 3C) can be explained by the stability analysis of the phase difference between the excUnit pair (Eq. 2). We can divide the coupling pairs into three groups: large, small, and intermediate weights. Pairs with large weights maintain a small and stable phase difference ($\Delta\theta \approx 0$). This ensures that the Hebbian potentiation term, $c\exp\left(-\gamma\left|\Delta\theta_{kj}\right|\right)$, and its relative position in the J_{ee} distribution $\hat{J}_{ee,kj}$ remain consistently high. Consequently, these couplings sustain a high $E[J_{ee}]_t$ with a very small $S[J_{ee}]_t$. Conversely, for pairs with small weights, the phases evolve almost independently of each other. Consequently, $S[J_{ee}]_t$ depends primarily on the natural frequency difference $\Delta\omega$. The largest $S[J_{ee}]_t$ was found in pairs with intermediate weights. In this regime, the intrinsic synchronizing force between the two units is closely counterbalanced by external driving influences, chiefly their natural frequency difference, $\Delta\omega$. Furthermore, Hebbian potentiation and homeostatic depression are also balanced. Small fluctuations in $\Delta\theta$ can frequently tip these balances and reverse the direction of the weight change, leading to large fluctuations in the coupling weight J_{ee}.

From a dynamics perspective, these mechanisms not only explain the characteristic bow-shaped distribution in Fig. 3C but also a key feature of biological synapses: larger synapses are more stable than smaller ones (38–40). Moreover, particularly in the desynchronized state, our model reproduces the relationship between the synaptic size and its changes reported in experimental studies (40, 41) (Fig. 3D and E, green lines; see Results). This alignment with detailed experimental trends further supports the notion that our model effectively captures synaptic dynamics.

The quasi-steady J_{ee} distribution is determined by the phase difference distribution (Fig. 1E, 1F, and SI Appendix, Fig. S1C and S1D), as it is a transformation of the $\Delta\theta$ distribution via the Hebbian function (Eq. 1). In this study, the exponential rule $c\exp\left(-\gamma\left|\Delta\theta_{kj}\right|\right)$ transforms the uniform phase difference distribution into a hyperbolic weight distribution (Appendix, Eq. S8–

12). This framework suggests that by modifying the Hebbian function, it is possible to generate the J_{ee} distribution into an arbitrary form, such as a log-normal distribution observed in the brain (12, 34, 35).

Eq. 2 further suggests that unit pairs with small natural frequency differences ($\Delta\omega$) and small initial phase differences ($\Delta\theta$) are more robust and more likely to return to a stable, synchronized state even after large perturbations. This explains the results shown in Figure 4, where a small $\Delta\omega$ and initial $\Delta\theta$ lead to stable and robust coupling. In our simulation setting (Fig. 1F, magenta circle), the Hebbian plasticity-induced enhancement of interaction strength near $\Delta\theta$=0 is limited, even though the plasticity slightly strengthens the restoring force near the stable point (Appendix, Fig. S3). Thus, the tendency for pairs with small $\Delta\omega$ and small initial $\Delta\theta$ to be more robust and stable arises primarily from the underlying sinusoidal form of the baseline interaction function rather than plasticity-induced modifications. This finding resonates with observations in the brain, where neurons that exhibit synchronized firing prior to learning (analogous to a small $\Delta\theta$) are more likely to be grouped into the same assembly during learning (60–62). However, it remains unclear whether these neurons also share similar intrinsic firing frequencies, which would correspond to a small $\Delta\omega$ in our model.

The fluctuation of J_{ee} when K_i is intermediate (Figs. 2–4, K_i=0.8, 1.0) can be attributed to the system dynamics becoming bistable and alternating between synchronization and desynchronization. This causes fluctuations in the phase distribution, which is the primary factor driving changes in J_{ee}. Furthermore, in this state, the periodic fluctuation of the order parameters R_{exc} and R_{inh} constantly changes in the interaction term, $F_{inh} - F_{exc}^{(-kj)}$ (Eq. 2). This dynamic instability also strongly perturbs the phase differences $\Delta\theta$ of moderately coupled pairs.

Limitations. While the Kuramoto model provides foundational insights, it is considerably simpler than actual neuronal behavior and has some limitations. First, our model simplifies neuronal interactions to mere attractive and repulsive forces, overlooking the pulse-like nature, interaction delay, and intricate coupling relationships of real neurons (63). Second, the model underrepresents the complexity of neuroplasticity, such as the influence of neurotransmitters and internal conditions (64), plasticity in inhibitory neurons (65, 66), and short-term plasticity, including adaptation (67). Lastly, the model does not distinguish between brain states, such as full wakefulness, NREM sleep, and REM sleep, which are believed to play unique roles in learning and neural reorganization (3, 4). Addressing these limitations is essential for a more accurate and comprehensive understanding of neural dynamics and plasticity.

Future directions. Future research can consider multiple directions to expand the system. In this study, we observed a behavior in which strong couplings were retained and intermediate couplings were randomly perturbed at low levels of inhibition. Creativity may require mechanisms for evaluating and stabilizing randomly reorganized circuits (58, 68). This mechanism is not yet fully understood; however, dopamine activity during rest (59) may be a key factor. Another important question is how changes in overall synchrony during sleep affect the interactions between functionally distinct networks, such as the hippocampus and cerebral cortex. Exploring the influence of synchrony transitions on interregional plasticity could shed light on how memory traces originally stored in the hippocampus gradually become integrated or transferred to cortical regions (69). Moreover, our model did not specifically consider the dimensionality of information; however, understanding how the brain represents and selects multidimensional information is crucial for cognition (70). We must consider the biases, interactions, and plasticity rules required to represent and select multidimensional information from the external world. Clarifying these mechanisms will contribute to a deeper understanding of how neural circuits are reorganized to support abstraction and creativity in the brain.

Materials and Methods

pEI-Kuramoto model. The original Kuramoto model (13, 14, 71) is expressed as:

$$\frac{d\theta_j(t)}{dt} = \omega_j + \frac{K}{N}\sum_{k}^{N} \sin\left(\theta_k(t) - \theta_j(t)\right) \quad \text{(M1)},$$

where $\theta_j(t)$ is the phase of unit *j* at time *t*, ω_j is the natural frequency of unit j following a probability distribution $g(\omega)$, *N* is the number of units, and *K* is the interaction strength among the oscillation units. In the original Kuramoto model, *K* is applied constantly and uniformly to all unit pairs. The order parameter *R* and the mean phase ψ are then calculated from the mean vector of the oscillators as:

$$Re^{i\psi} = \frac{1}{N}\sum_{j}^{N} e^{i\theta_j} \quad \text{(M2)},$$

where i denotes an imaginary unit. Given Euler's formula and Eq M2,

$$\frac{1}{N}\sum_{k}^{N} \sin(\theta_k - \theta_j) = \frac{1}{N}\sum_{k}^{N} \mathrm{Im}\left[e^{i\theta_k}e^{-i\theta_j}\right] = \mathrm{Im}\left[Re^{i\psi}e^{-i\theta_j}\right] = R\sin(\psi - \theta_j) \quad \text{(M3)}.$$

Considering Eq M3, Eq M1 becomes

$$\frac{d\theta_j}{dt} = \omega_j + KR\sin(\psi - \theta_j) \quad \text{(M4)}.$$

In our previous EI-Kuramoto model (16), the oscillation units were categorized into two groups: excitatory and inhibitory units, referred to as excUnits and inhUnits, respectively. Employing these terms clarified that the units in the model represented excitatory and inhibitory factors, distinguishing them from actual neurons or synapses. The interaction strength of the sine wave functions with zero phase lag is characterized by purely attractive interactions in excUnits and purely repulsive interactions in inhUnits. Hence, the terms "excitatory" and "inhibitory" are used interchangeably with "attractive" and "repulsive," respectively. The interaction strength *K* is divided into four quantifiable parameters: K_{ee} (attractive strength between excUnits), K_{ii} (repulsive strength between inhUnits), K_{ei} (attractive strength from excUnits to inhUnits), and K_{ie} (repulsive strength from inhUnits to excUnits). K_{ee}, K_{ii}, K_{ei}, and K_{ie} are distinct positive real numbers that are uniformly applicable across all the unit pairs. Consequently, Eq M4 becomes:

$$\frac{d\theta_{j,exc}}{dt} = \omega_{j,exc} + K_{ee}R_{exc}\sin(\psi_{exc} - \theta_{j,exc}) - K_{ie}R_{inh}\sin(\psi_{inh} - \theta_{j,exc}) \quad \text{(M5)}$$

for excUnits, and

$$\frac{d\theta_{j,inh}}{dt} = \omega_{j,inh} + K_{ei}R_{exc}\sin(\psi_{exc} - \theta_{j,inh}) - K_{ii}R_{inh}\sin(\psi_{inh} - \theta_{j,inh}) \quad \text{(M6)}$$

for inhUnits, where exc and inh represent the parameters for excUnits and inhUnits, respectively. The order parameter and mean phase of each excUnit and inhUnit are

$$R_{exc}e^{i\psi_{exc}} = \frac{1}{N_{exc}}\sum_{j}^{N_{exc}} e^{i\theta_{j,exc}} \quad \text{(M7)}$$

and

$$R_{inh}e^{i\psi_{inh}} = \frac{1}{N_{inh}}\sum_{j}^{N_{inh}} e^{i\theta_{j,inh}} \quad \text{(M8)}.$$

In the present study, we developed a pEI-Kuramoto model (Fig. 1A). A pivotal modification of our previous EI-Kuramoto model is that the constant and uniform interaction strength value K_{ee} is replaced with the heterogeneous and plastic coupling weight (interaction strength of an individual unit pair) matrix J_{ee}. The J_{ee} distribution is defined by its mean μ_{Jee} and standard deviation σ_{Jee}, which are scaled with the inverse of N_{exc} to adjust for the system size and to facilitate comparisons with other Kuramoto-model variants. Accordingly, the initial J_{ee} distribution follows the Gaussian distribution $g(J_{ee}) \sim \mathcal{N}(\hat{\mu}_{Jee}, (\hat{\sigma}_{Jee})^2)$, where $\hat{\mu}_{Jee} = \mu_{Jee}/\mathrm{N}_{exc}$, $\hat{\sigma}_{Jee} = \sigma_{Jee}/\mathrm{N}_{exc}$. The other interaction strengths, K_{ii}, K_{ei}, and K_{ie}, were uniform and consistently applicable across all units. Eq M5 becomes

$$\frac{d\theta_{j,exc}}{dt} = \omega_{j,exc} + \sum_{k}^{N_{exc}} J_{ee,kj} \sin\left(\theta_{k,exc} - \theta_{j,exc}\right) - K_{ie} R_{inh} \sin\left(\psi_{inh} - \theta_{j,exc}\right) \quad \text{(M9).}$$

$J_{ee,kj}$ is the coupling weight between the excUnits k (pre) and j (post).

Given the rotational symmetry, when the mean natural frequencies of excUnits and inhUnits are equal, $\bar{\omega} = \bar{\omega}_{exc} = \bar{\omega}_{inh}$, the mean natural frequencies can be set to 0 rad/s. This is equivalent to rotating a coordinate by the mean natural frequency $\bar{\omega}$ (71). For all simulations in this study: $N_{exc} = 80$, $N_{inh} = 20$; total simulation duration $T = 50$ s; time step $dt = 0.01$ s. The $g(\omega)$ followed the Gaussian distribution $g(\omega) \sim \mathcal{N}(0, 0.01)$ for both excUnits and inhUnits. In Figs. 2–5, K_{ii} and K_{ie} are unified with the same parameter K_i to simplify the simulation.

$$K_i = K_{ie} = K_{ii} \quad \text{(M10).}$$

At each time step Δt (= dt = 0.01 s in this study), the J_{ee} values were first modulated by Hebbian potentiation and then rescaled using homeostatic regularization rules. The Hebbian potentiation plasticity is implemented as an exponential function:

$$J_{Hebb} = J_{ee,kj}(t) + \alpha \exp\left(-\gamma |\Delta\theta_{kj}|\right) \quad \text{(M11).}$$

α is the learning rate for Hebbian plasticity. Note that α should scale proportionally with an inverse of N_{exc} as $\alpha \propto 1/N_{exc}$ to maintain consistency across different system sizes. γ determines the sharpness of the exponential decay from the peak. $\Delta\theta_{kj}$ is the phase difference between excUnit k and j

$$\Delta\theta_{kj} = \theta_{k,exc} - \theta_{j,exc} \left(-\pi \leq \Delta\theta_{kj} < \pi\right) \quad \text{(M12).}$$

The implementation of Hebbian plasticity with a cosine function (SI Appendix, Fig. S1A) is defined as

$$J_{Hebb} = J_{ee,kj}(t) + \frac{\alpha}{2}\{\cos\left(\Delta\theta_{kj}\right) + 1\} \quad \text{(M13).}$$

In any Hebbian learning rule in this paper, weight changes of $J_{ee,kj}$ and $J_{ee,jk}$ are the same due to the symmetry with respect to the sign of $\Delta\theta_{kj}$.

After the Hebbian modulations, J_{Hebb} was rescaled with the homeostatic regularization plasticity rule to prevent overpotentiation. Plasticity was implemented as follows:

$$\hat{J}_{Hebb} = \frac{\hat{\sigma}_{Jee}}{S[J_{Hebb}]_n}(J_{Hebb} - E[J_{Hebb}]_n) + \hat{\mu}_{Jee}$$

$$J_{ee,kj}(t + \Delta t) = \beta \hat{J}_{Hebb} + (1 - \beta) J_{Hebb} \quad \text{(M14).}$$

$\hat{J}_{Hebb}$ represents the normalized value (homeostatic set point) of J_{Hebb} under the initial setting of the mean $\hat{\mu}_{Jee}$ and standard deviation $\hat{\sigma}_{Jee}$. β is the learning rate for homeostatic plasticity. This procedure scales $J_{ee,kj}$ toward the initial targets, $\hat{\mu}_{Jee}$ and $\hat{\sigma}_{Jee}$.

The change in coupling weight at each time step ΔJ_{ee} (Fig. 3D and E) was defined as

$$\Delta J_{ee} = J_{ee}(t + \Delta t) - J_{ee}(t) \quad \text{(M15)}$$

For plotting, pairs of ΔJ_{ee} and $J_{ee}(t)$ values were pooled across all excUnit pairs and time points, and the J_{ee}(t) values were binned (bin size = 0.001).

Cyclic inhibitory modulation. In Fig. 5, K_i is modulated as a sine function

$$K_i = A_s \sin(\omega_s t) + C_s \quad \text{(M16),}$$

where A_s (= 0.32), ω_s (= 0.004π), and C_s (= 1.28) are the amplitude, frequency, and baseline constant for the sine modulation, respectively. The other parameters for interaction strengths are held constant to simplify the simulation: μ_{Jee} = 1, σ_{Jee} = 0.1, K_{ei} = 3, and T = 3,000 s.

Statistics. $E[\cdot]_t$ (also $E\{\cdot\}_t$) and $S[\cdot]_t$ are the mean and the standard deviation over time, respectively, where t indicates the number of time points. $E[\cdot]_n$ and $S[\cdot]_n$ are the mean and the standard deviation among unit pairs, respectively, where n indicates the number of unit pairs. $E[\cdot]_{t,n}$ and $S[\cdot]_{t,n}$ represent mean and standard deviation, respectively, pooling all values across time and unit pairs. Here, $\cdot$ represents a certain variable. The range of time for the time series analyses ($E[\cdot]_t$, $S[\cdot]_t$, $E[\cdot]_{t,n}$, and $S[\cdot]_{t,n}$) is [T/2, T] to exclude the initial

fluctuations. For Fig. 5B lower panel, value of $E\{S[J_{ee}]_t\}_n$ was estimated in the time window [-15s, +15 s] for each time point.

Descriptive statistics (mean, standard deviation, kurtosis, and skewness) and statistical tests were performed using the Python NumPy and SciPy libraries. The Dip test (36) was performed using the Python Diptest Library (https://github.com/RUrlus/diptest). The dip value is the maximum distance between the actual data distribution and the fitting result of the monomodal Gaussian distribution. If the data distribution is close to a monomodal Gaussian distribution, the dip value is low. If is bimodal, then its value is high. Hierarchical clustering was performed using the linkage function of the Python SciPy library.

Code Availability Statement. The scripts for this study can be found at Google Colaboratory: https://colab.research.google.com/drive/1v8JF97G9YdwUOh_Wuh9i_TvuGa42fLAu?usp=sharing

Acknowledgments.
We would like to thank Susumu Setogawa for his insightful comments on the manuscript. This study was supported by Japan Society for the Promotion of Science KAKENHI [grant 24K18243 to S.K.; grant 23H02788 to K.M.] and the Takeda Science Foundation [to K.M.]. The funding sources had no involvement in the study design, data collection, interpretation, or the decision to submit this paper for publication.

References

1. J. G. Jenkins, K. M. Dallenbach, Obliviscence during sleep and waking. *Am. J. Psychol.* **35**, 605 (1924).
2. G. Wallas, *The art of thought* (Jonathan Cape, 1926).
3. N. Landmann *et al.*, The reorganisation of memory during sleep. *Sleep Med. Rev.* **18**, 531–541 (2014).
4. P. A. Lewis, G. Knoblich, G. Poe, How memory replay in sleep boosts creative problem-solving. *Trends Cogn. Sci.* **22**, 491–503 (2018).
5. H. Norimoto, *et al.*, Hippocampal ripples down-regulate synapses. *Science* **359**, 1524–1527 (2018).
6. A. Goto, *et al.*, Stepwise synaptic plasticity events drive the early phase of memory consolidation. *Science* **374**, 857–863 (2021).
7. K. D. Harris, A. Thiele, Cortical state and attention. *Nat. Rev. Neurosci.* **12**, 509–523 (2011).
8. M. Steriade, R. R. Llinás, The functional states of the thalamus and the associated neuronal interplay. *Physiol. Rev.* **68**, 649–742 (1988).
9. B. Haider, M. Häusser, M. Carandini, Inhibition dominates sensory responses in the awake cortex. *Nature* **493**, 97–100 (2013).
10. H. Miyawaki, K. Diba, Regulation of hippocampal firing by network oscillations during sleep. *Curr. Biol.* **26**, 893–902 (2016).
11. H. Alfonsa, *et al.*, Intracellular chloride regulation mediates local sleep pressure in the cortex. *Nat. Neurosci.* **26**, 64–78 (2022).
12. K. Mizuseki, G. Buzsáki, Preconfigured, skewed distribution of firing rates in the hippocampus and entorhinal cortex. *Cell Rep.* **4**, 1010–1021 (2013).
13. Y. Kuramoto, *Chemical oscillations, waves, and turbulence* (Springer, 1984).
14. Y. Kuramoto, Self-entrainment of a population of coupled non-linear oscillators in *International Symposium on Mathematical Problems in Theoretical Physics*, (Springer, 1975), pp. 420–422.
15. E. Montbrió, D. Pazó, Kuramoto model for excitation-inhibition-based oscillations. *Phys. Rev. Lett.* **120**, 244101 (2018).
16. S. Kuroki, K. Mizuseki, Excitation-inhibition balance controls synchronization in a simple model of coupled phase oscillators. *Neural Comput.* **37**, 1353–1372 (2025).
17. D. O. Hebb, *The organization of behavior; a neuropsychological theory* (Wiley, 1949).
18. G. G. Turrigiano, The self-tuning neuron: synaptic scaling of excitatory synapses. *Cell* **135**, 422–435 (2008).

19. T. Toyoizumi, M. Kaneko, M. P. Stryker, K. D. Miller, Modeling the dynamic interaction of Hebbian and homeostatic plasticity. *Neuron* **84**, 497–510 (2014).
20. S. Kim, D. Jung, S. Royer, Place cell maps slowly develop via competitive learning and conjunctive coding in the dentate gyrus. *Nat. Commun.* **11**, 4550 (2020).
21. S. Benas, X. Fernandez, E. Kropff, Modeled grid cells aligned by a flexible attractor. *eLife* **12** (2024).
22. S. N. Weber, H. Sprekeler, Learning place cells, grid cells and invariances with excitatory and inhibitory plasticity. *Elife* **7**, e34560 (2018).
23. T. Aoki, T. Aoyagi, Co-evolution of phases and connection strengths in a network of phase oscillators. *Phys. Rev. Lett.* **102**, 034101 (2009).
24. J. C. Bronski, *et al.*, The stability of fixed points for a Kuramoto model with Hebbian interactions. *Chaos* **27**, 053110 (2017).
25. J. Fialkowski, *et al.*, Heterogeneous nucleation in finite-size adaptive dynamical networks. *Phys. Rev. Lett.* **130**, 067402 (2023).
26. S. Y. Ha, J. Lee, Z. Li, J. Park, Emergent dynamics of Kuramoto oscillators with adaptive couplings: Conservation law and fast learning. *SIAM J. Appl. Dyn. Syst.* **17**, 1560–1588 (2018).
27. S. Y. Ha, S. E. Noh, J. Park, Synchronization of Kuramoto oscillators with adaptive couplings. *SIAM J. Appl. Dyn. Syst.* **15**, 162–194 (2016).
28. R. K. Niyogi, L. Q. English, Learning-rate-dependent clustering and self-development in a network of coupled phase oscillators. *Phys. Rev. E Stat. Nonlin. Soft Matter Phys.* **80**, 066213 (2009).
29. J. Park, D. Poyato, J. Soler, Filippov trajectories and clustering in the Kuramoto model with singular couplings. *J. Eur. Math. Soc.* **23**, 3193–3278 (2021).
30. C. B. Picallo, H. Riecke, Adaptive oscillator networks with conserved overall coupling: Sequential firing and near-synchronized states. *Phys. Rev. E Stat. Nonlin. Soft Matter Phys.* **83**, 036206 (2011).
31. D. Poyato, Filippov flows and mean-field limits in the kinetic singular Kuramoto model. *arXiv [math.AP]* (2019).
32. Q. Ren, J. Zhao, Adaptive coupling and enhanced synchronization in coupled phase oscillators. *Phys. Rev. E Stat. Nonlin. Soft Matter Phys.* **76**, 016207 (2007).
33. P. Seliger, S. C. Young, L. S. Tsimring, Plasticity and learning in a network of coupled phase oscillators. *Phys. Rev. E Stat. Nonlin. Soft Matter Phys.* **65**, 041906 (2002).
34. G. Buzsáki, K. Mizuseki, The log-dynamic brain: how skewed distributions affect network operations. *Nat. Rev. Neurosci.* **15**, 264–278 (2014).
35. M. Iwase, K. Diba, E. Pastalkova, K. Mizuseki, Dynamics of spike transmission and suppression between principal cells and interneurons in the hippocampus and entorhinal cortex. *Hippocampus* **34**, 393–421 (2024).
36. J. A. Hartigan, P. M. Hartigan, The dip test of unimodality. *Ann. Stat.* **13**, 70–84 (1985).
37. A. C. Nobre, S. Kastner, Eds., *The Oxford Handbook of Attention* (Oxford University Press, 2014).
38. A. J. G. D. Holtmaat, *et al.*, Transient and persistent dendritic spines in the neocortex in vivo. *Neuron* **45**, 279–291 (2005).
39. J. Grutzendler, N. Kasthuri, W.-B. Gan, Long-term dendritic spine stability in the adult cortex. *Nature* **420**, 812–816 (2002).
40. N. Yasumatsu, M. Matsuzaki, T. Miyazaki, J. Noguchi, H. Kasai, Principles of long-term dynamics of dendritic spines. *J. Neurosci.* **28**, 13592–13608 (2008).
41. Y. Loewenstein, A. Kuras, S. Rumpel, Multiplicative dynamics underlie the emergence of the log-normal distribution of spine sizes in the neocortex in vivo. *J. Neurosci.* **31**, 9481–9488 (2011).
42. K. Okuda, Y. Kuramoto, Mutual entrainment between populations of coupled oscillators. *Progr. Theoret. Phys.* **86**, 1159–1176 (1991).
43. E. A. Martens, C. Bick, M. J. Panaggio, Chimera states in two populations with heterogeneous phase-lag. *Chaos* **26**, 094819 (2016).
44. D.-P. Yang, L. McKenzie-Sell, A. Karanjai, P. A. Robinson, Wake-sleep transition as a noisy bifurcation. *Phys. Rev. E.* **94**, 022412 (2016).

45. V. Priesemann, M. Valderrama, M. Wibral, M. Le Van Quyen, Neuronal avalanches differ from wakefulness to deep sleep--evidence from intracranial depth recordings in humans. *PLoS Comput. Biol.* **9**, e1002985 (2013).
46. K. B. Hengen, W. L. Shew, Is criticality a unified setpoint of brain function? *Neuron* **113**, 2582–2598.e2 (2025).
47. L. Parrino, R. Ferri, O. Bruni, M. G. Terzano, Cyclic alternating pattern (CAP): the marker of sleep instability. *Sleep Med. Rev.* **16**, 27–45 (2012).
48. D. Levenstein, G. Buzsáki, J. Rinzel, NREM sleep in the rodent neocortex and hippocampus reflects excitable dynamics. *Nat. Commun.* **10**, 2478 (2019).
49. D. Jercog, *et al.*, UP-DOWN cortical dynamics reflect state transitions in a bistable network. *Elife* **6**, e22425 (2017).
50. A. Lüthi, M. Nedergaard, Anything but small: Microarousals stand at the crossroad between noradrenaline signaling and key sleep functions. *Neuron* **113**, 509–523 (2025).
51. G. Tononi, C. Cirelli, Sleep and synaptic down-selection. *Eur. J. Neurosci.* **51**, 413–421 (2020).
52. H. Kasai, *et al.*, Learning rules and persistence of dendritic spines. *Eur. J. Neurosci.* **32**, 241–249 (2010).
53. L. Bollmann, P. Baracskay, F. Stella, J. Csicsvari, Sleep stages antagonistically modulate reactivation drift. *Neuron* **113**, 1446-1459.e6 (2025).
54. Y. Ziv, *et al.*, Long-term dynamics of CA1 hippocampal place codes. *Nat. Neurosci.* **16**, 264–266 (2013).
55. S. P. Vaidya, G. Li, R. A. Chitwood, Y. Li, J. C. Magee, Formation of an expanding memory representation in the hippocampus. *Nat. Neurosci.* **28**, 1510–1518 (2025).
56. B. Bartoldson, A. Morcos, A. Barbu, G. Erlebacher, The generalization-stability tradeoff in neural network pruning in *Advances in Neural Information Processing Systems*, H. Larochelle, M. Ranzato, R. Hadsell, M. F. Balcan, H. Lin, Eds. (Curran Associates, Inc., 2020), pp. 20852–20864.
57. T. Hoefler, D. Alistarh, T. Ben-Nun, N. Dryden, A. Peste, Sparsity in deep learning: pruning and growth for efficient inference and training in neural networks. *J. Mach. Learn. Res.* **22**, 10882–11005 (2021).
58. D. T. Campbell, Blind variation and selective retention in creative thought as in other knowledge processes. *Psychol. Rev.* **67**, 380–400 (1960).
59. S. N. Gomperts, F. Kloosterman, M. A. Wilson, VTA neurons coordinate with the hippocampal reactivation of spatial experience. *Elife* **4**, e05360 (2015).
60. G. Dragoi, S. Tonegawa, Preplay of future place cell sequences by hippocampal cellular assemblies. *Nature* **469**, 397–401 (2011).
61. A. Luczak, P. Barthó, K. D. Harris, Spontaneous events outline the realm of possible sensory responses in neocortical populations. *Neuron* **62**, 413–425 (2009).
62. J.-E. K. Miller, I. Ayzenshtat, L. Carrillo-Reid, R. Yuste, Visual stimuli recruit intrinsically generated cortical ensembles. *Proc. Natl. Acad. Sci. U. S. A.* **111**, E4053-E4061 (2014).
63. E. M. Izhikevich, *Dynamical systems in neuroscience: The geometry of excitability and bursting* (MIT Press, 2010).
64. Z. Brzosko, S. B. Mierau, O. Paulsen, Neuromodulation of spike-timing-dependent plasticity: Past, present, and future. *Neuron* **103**, 563–581 (2019).
65. Y. K. Wu, C. Miehl, J. Gjorgjieva, Regulation of circuit organization and function through inhibitory synaptic plasticity. *Trends Neurosci.* **45**, 884–898 (2022).
66. C. Q. Chiu, A. Barberis, M. J. Higley, Preserving the balance: diverse forms of long-term GABAergic synaptic plasticity. *Nat. Rev. Neurosci.* **20**, 272–281 (2019).
67. D. M. Blitz, K. A. Foster, W. G. Regehr, Short-term synaptic plasticity: a comparison of two synapses. *Nat. Rev. Neurosci.* **5**, 630–640 (2004).
68. R. E. Beaty, M. Benedek, P. J. Silvia, D. L. Schacter, Creative cognition and brain network dynamics. *Trends Cogn. Sci.* **20**, 87–95 (2016).
69. J. G. Klinzing, N. Niethard, J. Born, Mechanisms of systems memory consolidation during sleep. *Nat. Neurosci.* **22**, 1598–1610 (2019).
70. O. Barak, Recurrent neural networks as versatile tools of neuroscience research. *Curr. Opin. Neurobiol.* **46**, 1–6 (2017).

71. J. A. Acebrón, L. L. Bonilla, C. J. Pérez Vicente, F. Ritort, R. Spigler, The Kuramoto model: A simple paradigm for synchronization phenomena. *Rev. Mod. Phys.* **77**, 137–185 (2005).

Figures and Tables

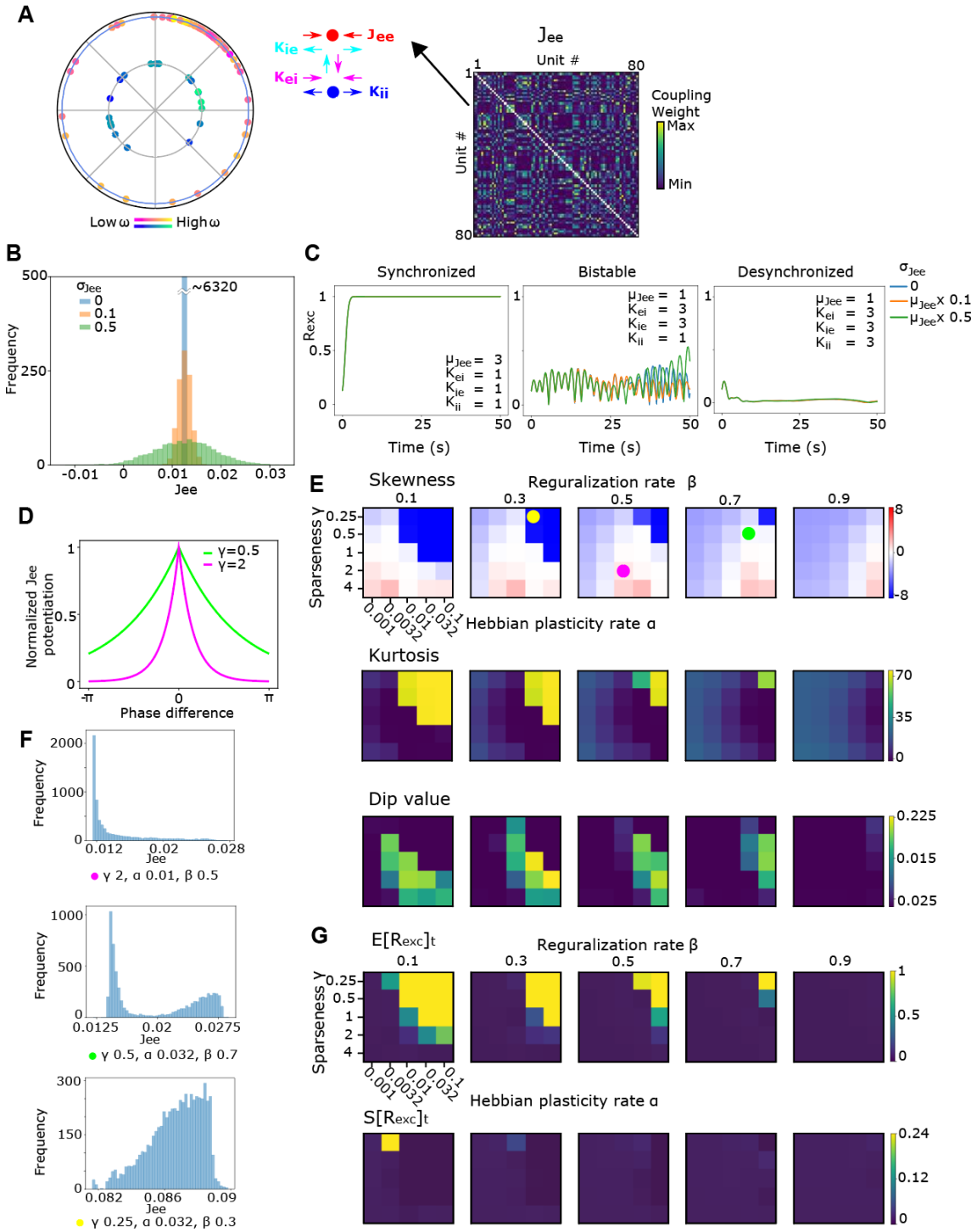

Figure 1. EI-Kuramoto model with distributed J_{ee} and plasticity

(A) Schematic representation of the pEI-Kuramoto model

Left: Oscillator units are excitatory (warm-colored) or inhibitory (cool-colored), each with its own natural frequency (shown by color gradients). Middle: J_{ee} functions attractively between excUnits (red arrows). K_{ei} is the attractive interaction strength from excUnit to inhUnit (magenta arrow). K_{ii} represents the repulsive strength between inhUnits (blue arrows). K_{ie} is the repulsive strength from inhUnit to excUnit (cyan arrow). K_{ei}, K_{ii}, and K_{ie} are constants that are applied uniformly across all units. Right: Each J_{ee} unit pair has its own coupling weight and undergoes plastic modification. (B) Distribution of J_{ee} coupling weights with different σ_{Jee}. μ_{Jee} = 1, N_{exc} = 80. (C) R_{exc} time traces of synchronized, bistable, and desynchronized states

with each σ_{Jee} and no plasticity. (D) Exponential rules of Hebbian potentiation plasticity. The J_{ee} weight of each pair of units is potentiated based on the phase difference between the units. (E) Evaluation of the J_{ee} distribution at the last frame (t = 50 s) with various plasticity parameters. Skewness (top panels), kurtosis (middle), and dip values (bottom). (F) J_{ee} distribution of exponential Hebbian plasticity rules at the last frame (t = 50 s) with various parameter settings. The parameter settings of the top, middle, and bottom panels correspond to those marked by magenta, green, and yellow circles in (E). (G) Evaluation of state synchrony with various plasticity parameters. $E[R_{exc}]_t$ and $S[R_{exc}]_t$ denote the time-averaged mean and standard deviation, respectively, of the order parameter for excUnits, R_{exc}. The parameters used for evaluation were N_{exc} = 80, N_{inh} = 20, μ_{Jee} = 1, σ_{Jee} = 0.1, K_{ei} = 3, K_{ie} = 3, K_{ii} = 3, corresponding to a desynchronized state of the system without plasticity (E–G).

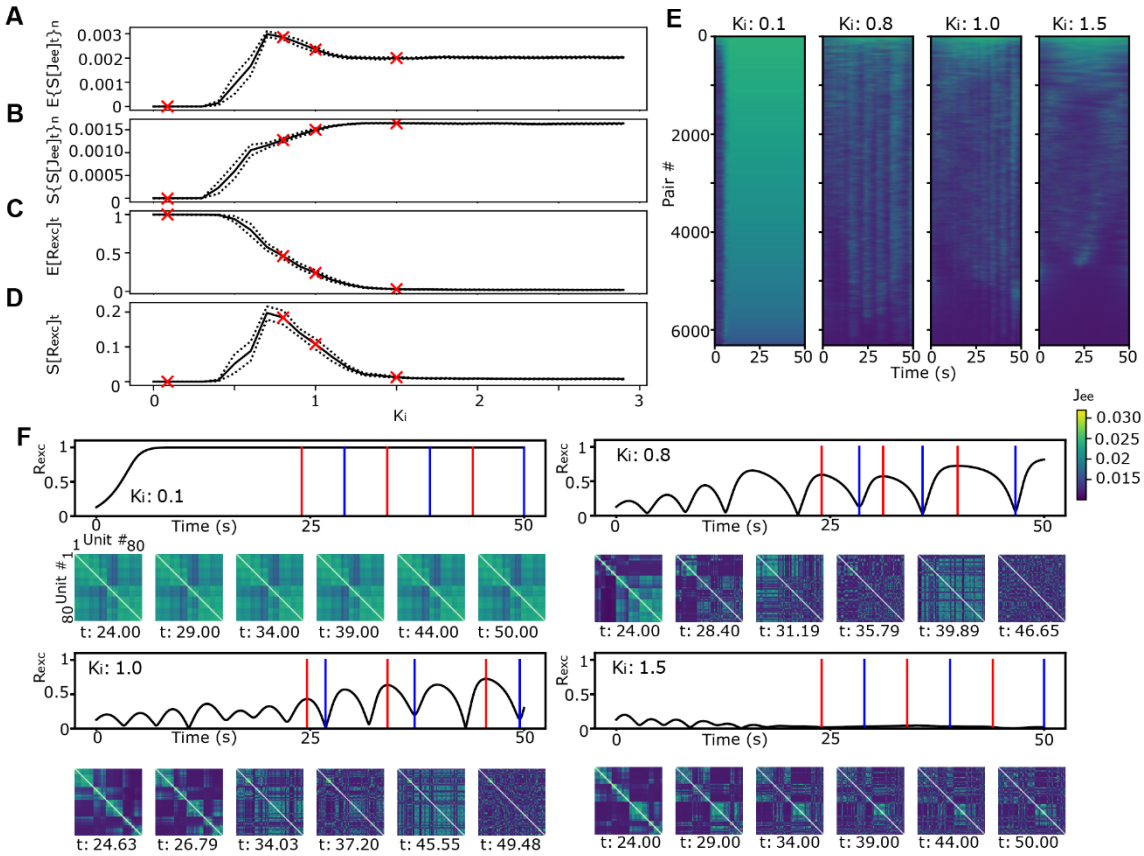

Figure 2. Changes in J_{ee} fluctuation with K_i modification

(A–D) (A) E{S[J_{ee}]$_t$}$_n$, (B) S{S[J_{ee}]$_t$}$_n$, (C) E[R_{exc}]$_t$, and (D) S[R_{exc}]$_t$ as a function of K_i. Red crosses indicate each value in the K_i conditions shown in (E) and (F). (E) Time course of J_{ee} weights under different K_i conditions. The order of unit pairs is sorted by E[J_{ee}]$_t$ for each K_i value. (F) Upper panels show R_{exc} traces. The lower panels show the J_{ee} weight matrix at selected time points indicated by the red and blue vertical lines in the top panels (red and blue are local maximum and local minimum, respectively, for K_i = 0.8 and 1.0; t = 24, 29, 34, 39, 44, and 50 for K_i = 0.1 and 1.5). The order of units is rearranged by the result of hierarchical clustering for the leftmost panel (around t: 24-25). E and F share the color bar. μ_{Jee} = 1, σ_{Jee} = 0.1, K_{ei} = 3, α = 0.01, β = 0.5, γ = 2.

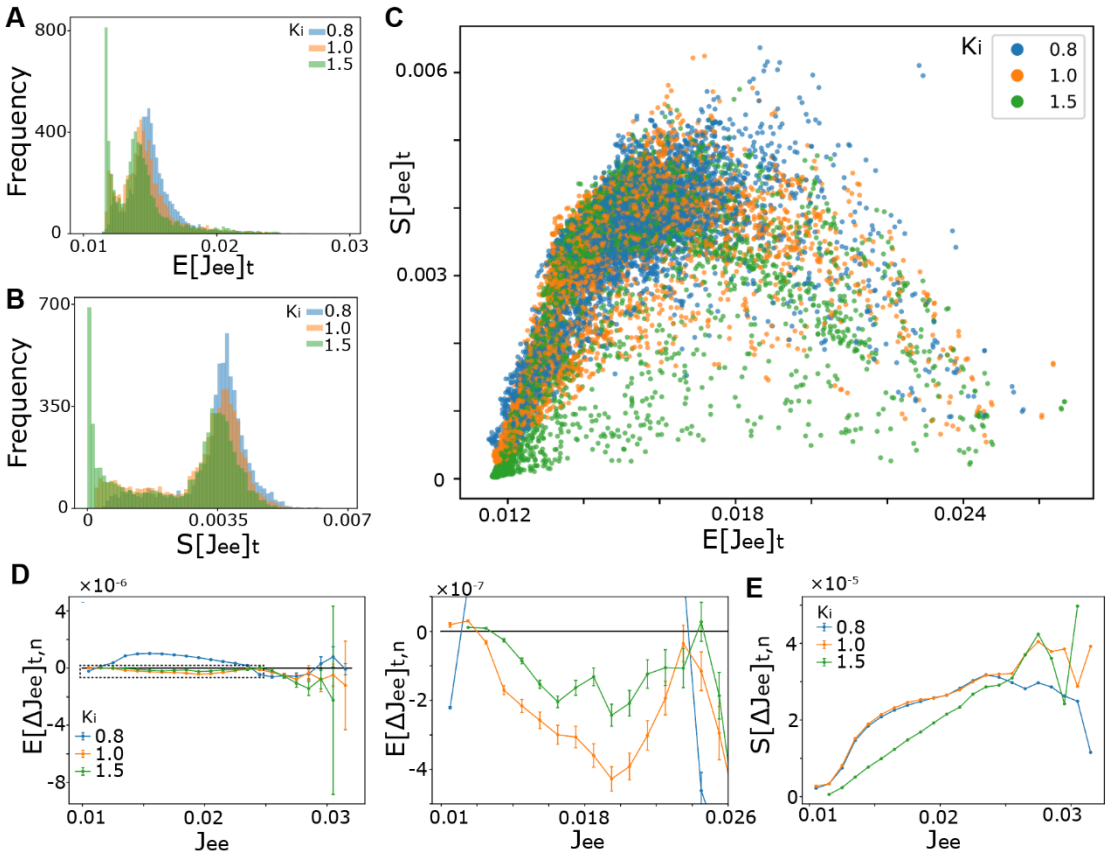

Figure 3. Relationship between the magnitude and fluctuation of J_{ee}

(A) E[J_{ee}]$_t$ histogram. (B) S[J_{ee}]$_t$ histogram. (C) E[J_{ee}]$_t$ vs. S[J_{ee}]$_t$ scatter plot for different K_i values. (D) E[ΔJ_{ee}]$_{t,n}$ as a function of J_{ee} for different K_i values. The right panel shows an enlarged view of the region enclosed by the dotted rectangle in the left panel. Black line indicates E[ΔJ_{ee}]$_{t,n}$ = 0. Error bars indicate the standard error of the mean (SEM). (E) S[ΔJ_{ee}]$_{t,n}$ as a function of J_{ee} for different K_i values. At each time point, all pairs of ΔJ_{ee} and the immediately preceding J_{ee} values were collected, binned by the J_{ee} values, and used to compute the statistics within each bin (D, E). μ_{Jee} = 1, σ_{Jee} = 0.1, K_{ei} = 3, α = 0.01, β = 0.5, γ = 2.

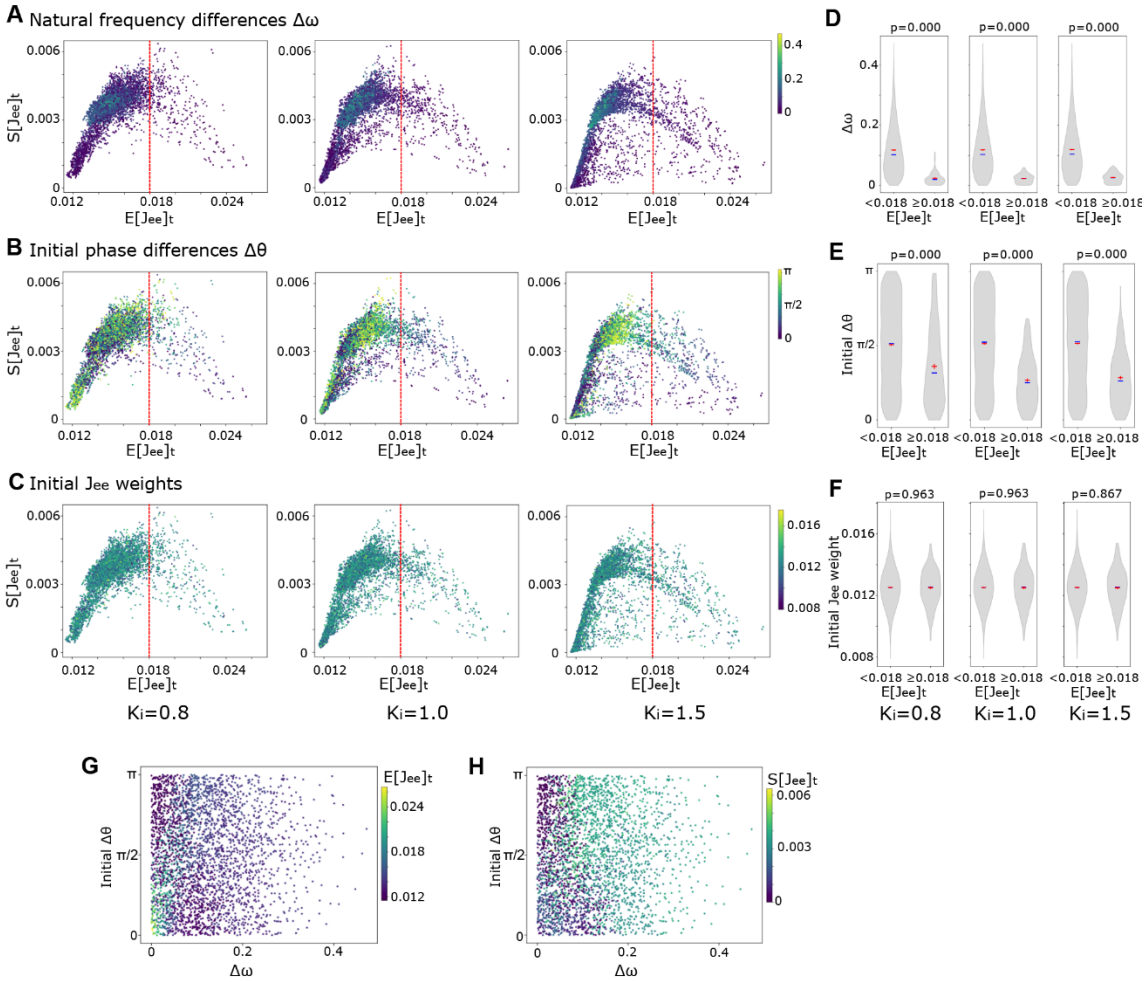

Figure 4. Factors affecting the J_{ee} fluctuation

(A–C) E[J_{ee}]t vs. S[J_{ee}]t scatter plot with color coding of (A) the natural frequency difference $\Delta\omega$, (B) the initial phase difference $\Delta\theta$, and (C) the initial J_{ee} weight over different K_i. The red dotted line for each panel indicates E[J_{ee}]t = 0.018. Left column, K_i = 0.8; middle column, K_i = 1.0; right column, K_i = 1.5.

(D–F) Violin plots provide distribution densities based on whether the threshold E[J_{ee}]t ≥ 0.18 or not for (D) natural frequency differences $\Delta\omega$, (E) initial phase differences $\Delta\theta$, and (F) initial J_{ee} weights across different K_i. The red and blue horizontal lines indicate the mean and median values, respectively. The red vertical lines indicate the standard errors. The numbers in the upper right corner of each panel are the p-values from the Mann–Whitney U-test. The numbers of unit pairs were as follows: for K_i = 0.8, E[J_{ee}]t < 0.018: n = 5968, E[J_{ee}]t ≥ 0.018: n = 352; for K_i = 1.0, E[J_{ee}]t < 0.018: n = 5920, E[J_{ee}]t ≥ 0.018: n = 400; for K_i = 1.5, E[J_{ee}]t < 0.018: n = 5852, E[J_{ee}]t ≥ 0.018: n = 468. The statistics were as follows: (D, natural frequency difference), K_i = 0.8, z = 24.7, p < 0.001; K_i = 1.0, z = 26.8, p < 0.001; K_i = 1.5, z = 27.8, p < 0.001. (E, initial phase difference) K_i = 0.8, z = 9.20, p < 0.001; K_i = 1.0, z = 16.4, p < 0.001; K_i = 1.5, z = 16.7, p < 0.001. (F, initial J_{ee} weight) K_i = 0.8, z = –0.046, p = 0.96; K_i = 1.0, z = 0.046, p = 0.96; K_i = 1.5, z = 0.17, p = 0.87.

(G and H) Scatter plots of natural frequency differences $\Delta\omega$ and initial phase differences $\Delta\theta$ with color coding of (G) E[J_{ee}]t and (H) S[J_{ee}]t (K_i = 1.5).

μ_{Jee} = 1, σ_{Jee} = 0.1, K_{ei} = 3, α = 0.01, β = 0.5, γ = 2.

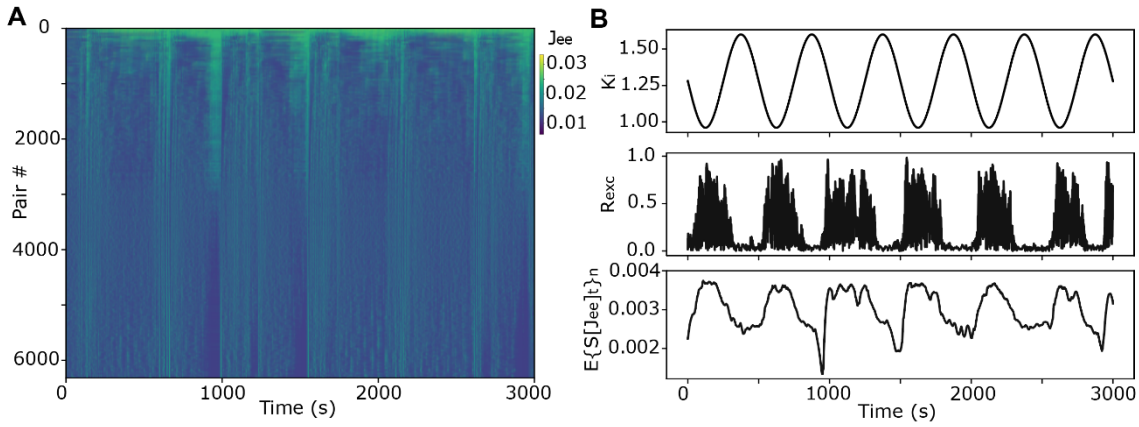

Figure 5. J_{ee} fluctuation changes with K_i cyclic modulation
(A) Time trace of each J_{ee} weight sorted by $E[J_{ee}]_t$. (B) Time traces of (top) K_i modulation, (middle) R_{exc}, and (low) $E\{S[J_{ee}]_t\}_n$. $\mu_{Jee} = 1$, $\sigma_{Jee} = 0.1$, $K_{ei} = 3$, $\alpha = 0.01$, $\beta = 0.5$, $\gamma = 2$.

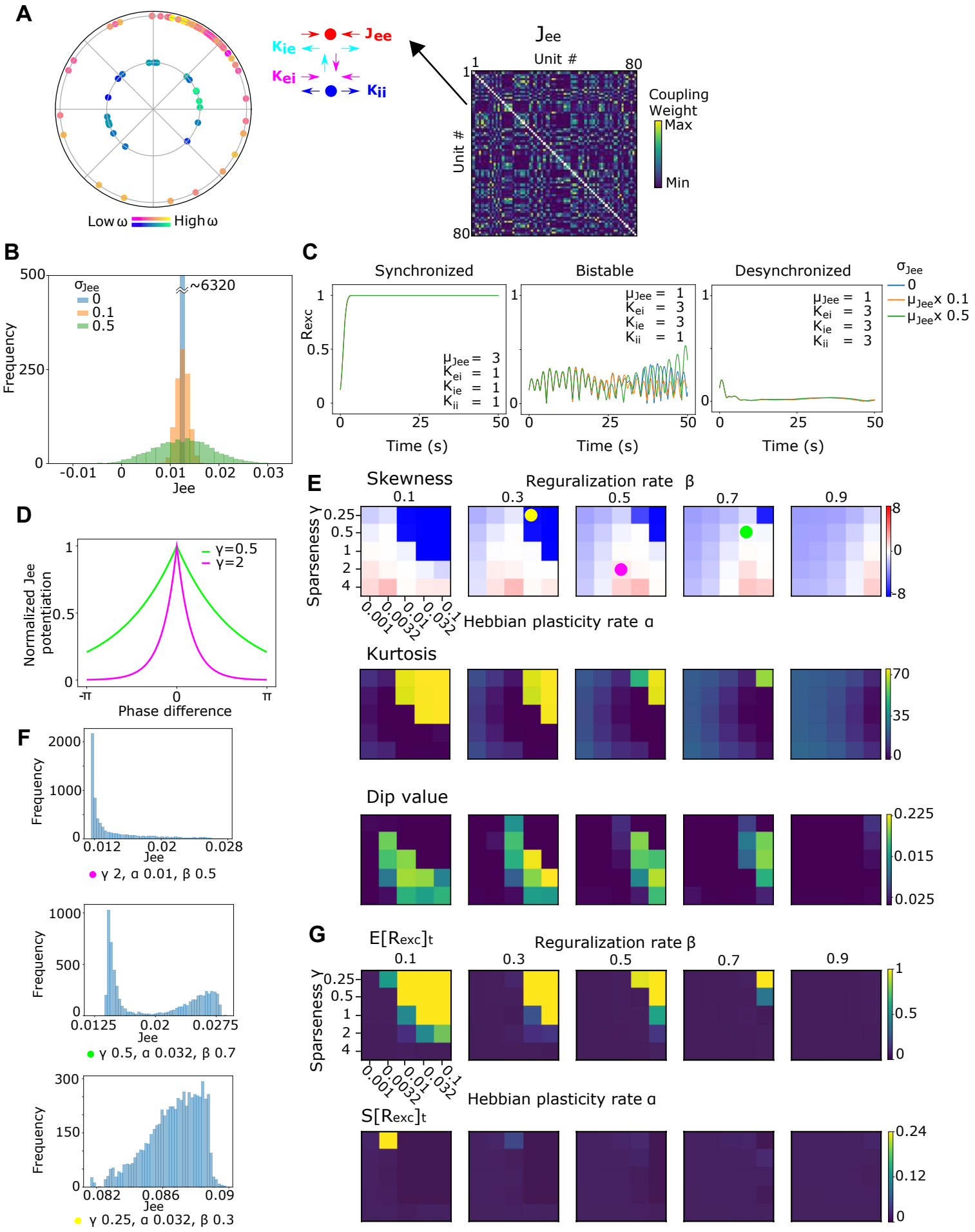
A
Low ω
High ω
Kie
Jee
Kei
Kii
Jee
Unit #
1
80
Coupling Weight
Max
Min
B
Frequency
σJee
0
0.1
0.5
~6320
Jee
C
Synchronized
Bistable
Desynchronized
Rexc
Time (s)
μJee = 3
Kei = 1
Kie = 1
Kii = 1
μJee = 1
Kei = 3
Kie = 3
Kii = 1
μJee = 1
Kei = 3
Kie = 3
Kii = 3
σJee
0
μJee x 0.1
μJee x 0.5
D
Normalized Jee potentiation
γ=0.5
γ=2
Phase difference
E
Skewness
Reguralization rate β
Sparseness γ
Hebbian plasticity rate α
Kurtosis
Dip value
F
Frequency
Jee
γ 2, α 0.01, β 0.5
γ 0.5, α 0.032, β 0.7
γ 0.25, α 0.032, β 0.3
G
E[Rexc]t
S[Rexc]t

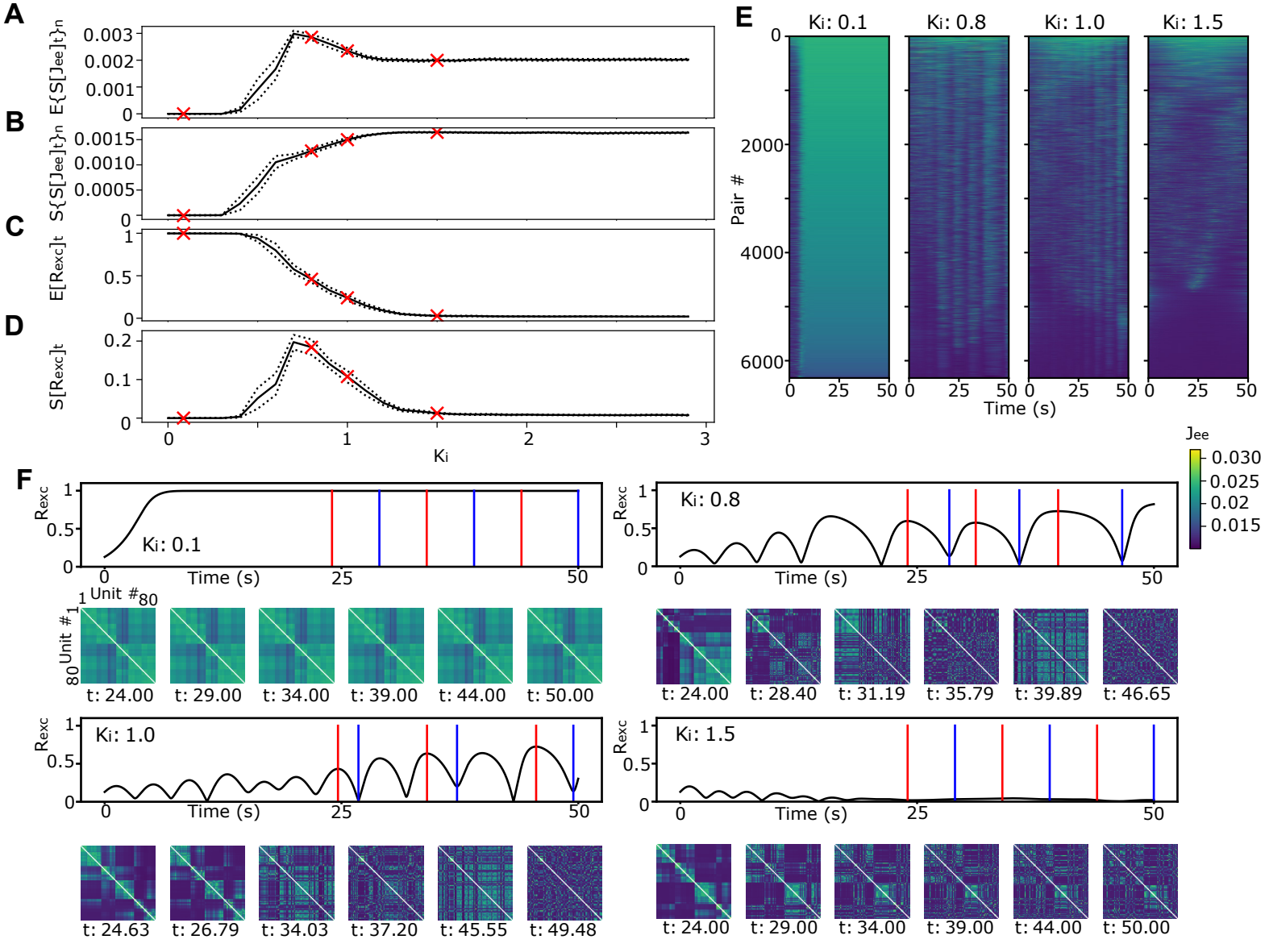
A
E{S[Jee]t}n
0.003
0.002
0.001
0
B
S{S[Jee]t}n
0.0015
0.0010
0.0005
0
C
E[Rexc]t
1
0.5
0
D
S[Rexc]t
0.2
0.1
0
0
1
2
3
Ki
E
Ki: 0.1
Ki: 0.8
Ki: 1.0
Ki: 1.5
Pair #
0
2000
4000
6000
0
25
50
Time (s)
Jee
0.030
0.025
0.02
0.015
F
Rexc
Ki: 0.1
Time (s)
Unit #
1
80
t: 24.00
t: 29.00
t: 34.00
t: 39.00
t: 44.00
t: 50.00
Ki: 0.8
t: 24.00
t: 28.40
t: 31.19
t: 35.79
t: 39.89
t: 46.65
Ki: 1.0
t: 24.63
t: 26.79
t: 34.03
t: 37.20
t: 45.55
t: 49.48
Ki: 1.5
t: 24.00
t: 29.00
t: 34.00
t: 39.00
t: 44.00
t: 50.00

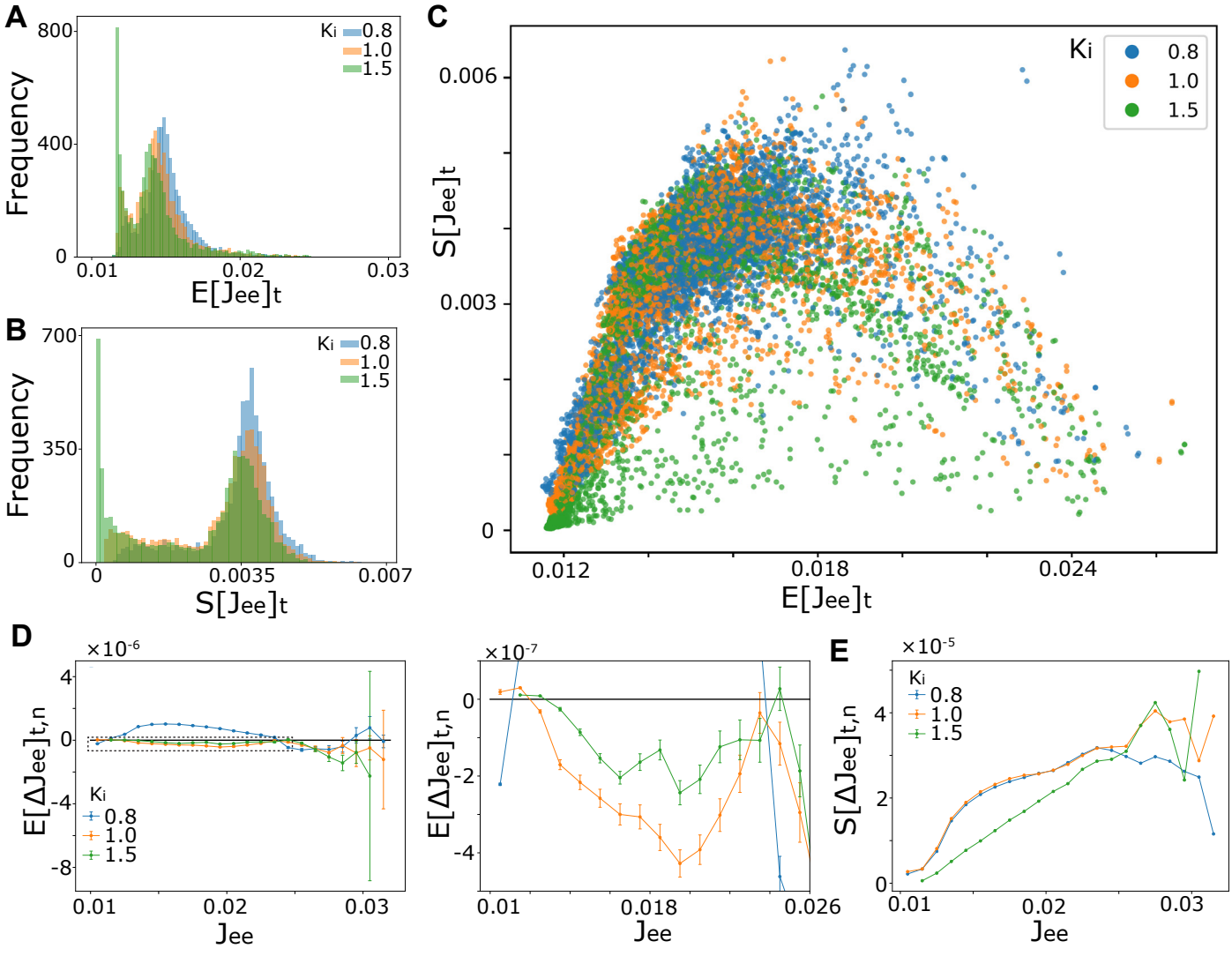
A
Frequency
E[Jee]t
Ki
0.8
1.0
1.5
B
Frequency
S[Jee]t
C
S[Jee]t
E[Jee]t
D
E[ΔJee]t,n
Jee
E
S[ΔJee]t,n

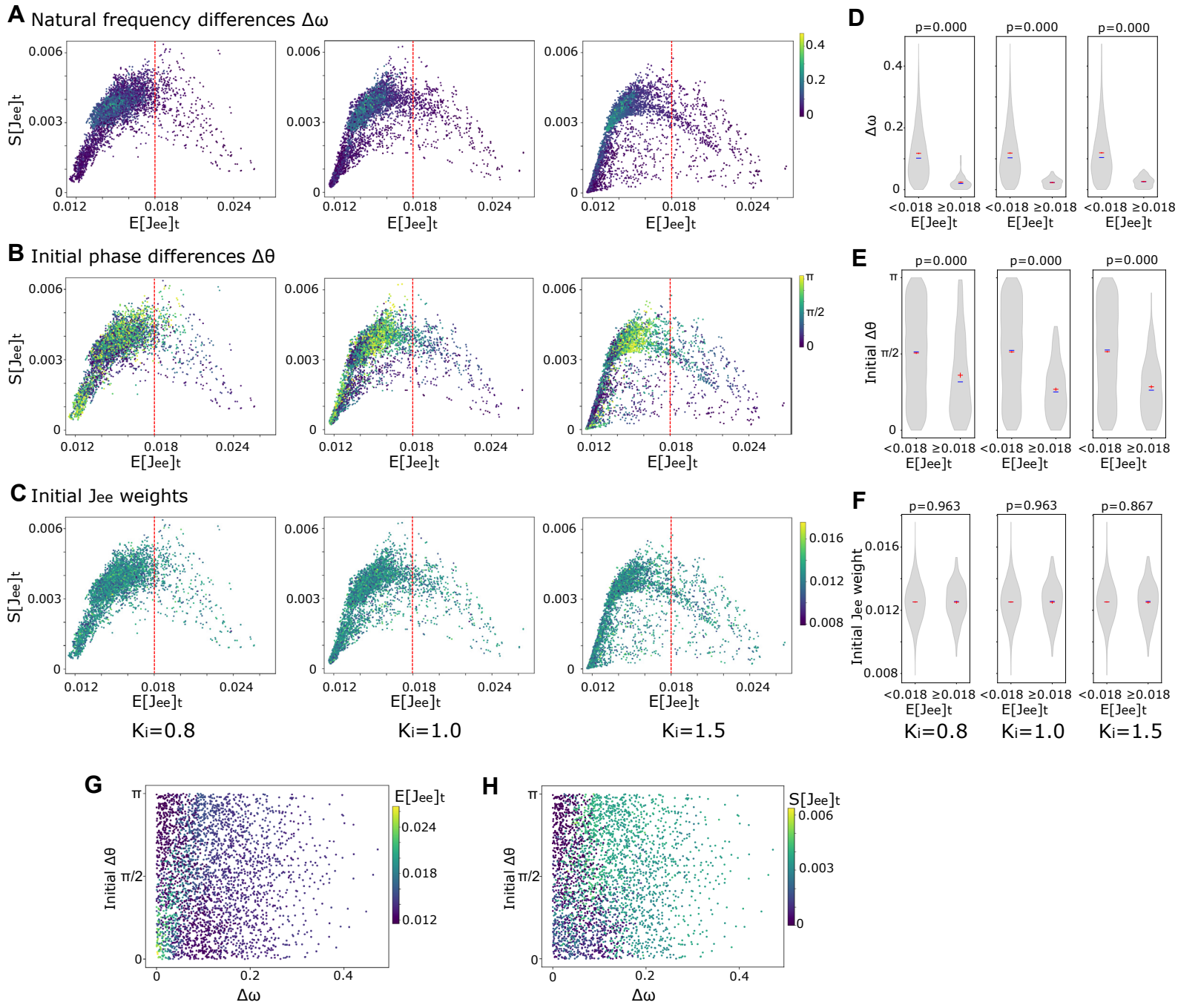
A Natural frequency differences Δω
B Initial phase differences Δθ
C Initial Jee weights
S[Jee]t
E[Jee]t
Ki=0.8
Ki=1.0
Ki=1.5
D
E
F
p=0.000
p=0.963
p=0.867
Δω
Initial Δθ
Initial Jee weight
<0.018 ≥0.018
G
H
Initial Δθ
Δω
E[Jee]t
S[Jee]t

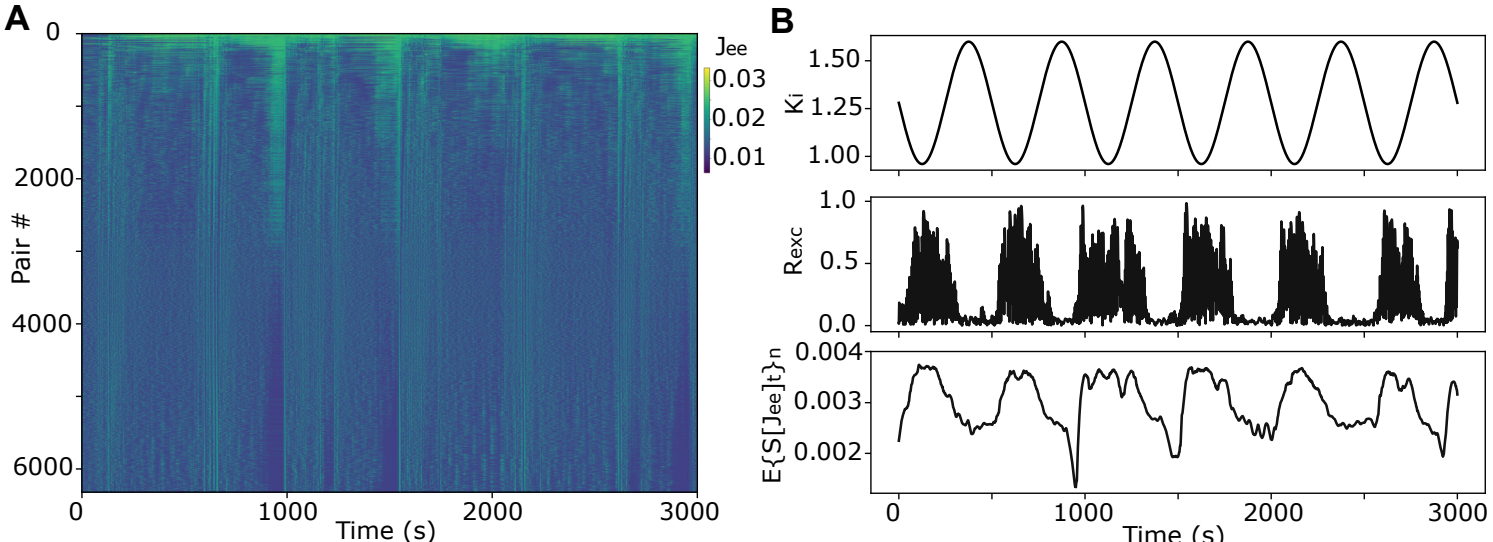
A
0
2000
4000
6000
Pair #
0
1000
2000
3000
Time (s)
Jee
0.03
0.02
0.01
B
1.50
1.25
1.00
Ki
1.0
0.5
0.0
Rexc
0.004
0.003
0.002
E{S[Jee]t}n
0
1000
2000
3000
Time (s)